PNAS Nexus, 2025, 4, pgae571
https://doi.org/10.1093/pnasnexus/pgae571
Advance access publication 23 December 2024
Research Report

Canopy elastic turbulence: Insights and analogies to canopy inertial turbulence

Ricardo Arturo Lopez de la Cruz [a,*], Simon J. Haward [a] and Amy Q. Shen [a]

[a]Micro/Bio/Nanofluidics Unit, Okinawa Institute of Science and Technology Graduate University, Onna-son, Okinawa 904-0495, Japan
*To whom correspondence should be addressed: Email: ricardo.lopez@oist.jp
Edited By Gary Grest

Abstract

Canopy flows occur when a moving fluid encounters a matrix of free-standing obstacles and are found in diverse systems, from forests and marine ecology to urban landscapes and biology (e.g. cilia arrays). In large-scale systems, involving Newtonian fluids (like water or air), canopy flows typically exhibit inertial turbulence due to high Reynolds numbers (Re). However, in small-scale systems like cilia, where Re is low, but the fluid can be viscoelastic (like mucus), the relevant control parameter is the Weissenberg number (Wi), quantifying elastic stresses in the flow. Here, we investigate the flow of a viscoelastic polymer solution over a microscopic canopy within a microfluidic device. As the Weissenberg number increases, the flow undergoes distinct transitions, eventually becoming unstable beyond a critical Wi. At high Wi, we observe the emergence of elastic turbulence (ET), a chaotic flow regime that, despite differing underlying mechanisms, exhibits striking similarities to large-scale canopy inertial turbulence. Similar to canopy inertial turbulence, ET within the canopy can be spatially divided into distinct regions: a porous layer within the canopy, a mixing layer at the canopy tips, a transitional region just above the canopy, and a Poiseuille-like flow further up. The separation of the flow into different regions reveals a new analogy between inertial turbulence and ET, providing a fresh insight into ET flows and expanding their potential for innovative microfluidic designs and real-world applications.

Keywords: canopy flow, elastic turbulence, viscoelastic flows, microfluidics, inertial canopy flow

Significance Statement

Until recently, it was thought that turbulence only occurred in inertial flows at high Reynolds numbers. However, even when inertia is negligible, the elasticity of fluids like mucus or blood can elicit a similar chaotic flow state called elastic turbulence (ET). ET is less well understood than classical turbulence. We study ET within a microscopic canopy, an array of slender obstacles mimicking structures like cilia in our bodies. We demonstrate that ET exhibits distinct flow regions and coherent structures analogous to those observed in large-scale inertial canopy flows, like forest canopies. This finding bridges the gap between classical and ET, offering new insights that could inspire innovative microfluidic designs, harnessing ET's chaotic behavior for enhanced mixing and flow control.

Introduction

The dynamics of canopy flows play a crucial role in a wide range of natural and engineered systems, influencing the distribution of nutrients, humidity, temperature, and more within environments such as forests, marine ecosystems, agricultural fields, and urban areas (1–6). Canopy flows at such large scales typically exhibit turbulence due to high Reynolds numbers (Re), a parameter reflecting the balance between inertial and viscous forces. We refer to these as *inertial* canopy flows. However, canopy flows also occur on much smaller scales, such as on cilia-covered surfaces within human and animal bodies (7–9) or around microorganisms (10). In these *micro*canopies, where Re is low and the fluid is often viscoelastic, the Weissenberg number (Wi) becomes the critical parameter. Wi compares the fluid's elastic stress to its viscous stress, and at high Wi, the flow can become unstable, transitioning into a chaotic regime known as elastic turbulence (ET) (11–13). ET is a turbulent-like flow, not exclusive to microcanopies, arising from entirely different mechanisms than classical turbulence as ET is driven by fluid elasticity rather than inertia (14, 15).

Recent advances have revealed intriguing parallels between the ET regime and classical inertial turbulence, such as increased flow resistance (14, 16), enhanced mixing (17), improved heat exchange (18, 19), a power-law decay of the energy spectrum in the frequency domain (14, 16, 20–25), and features of intermittency and multifractality (26). Additionally, Monami-like waves have been observed in microcanopies (27), further highlighting the similarities between ET and classical turbulence. These findings suggest that the behavior of ET can be better understood by

Competing Interest: The authors declare no competing interests.
Received: September 13, 2024. **Accepted:** December 16, 2024

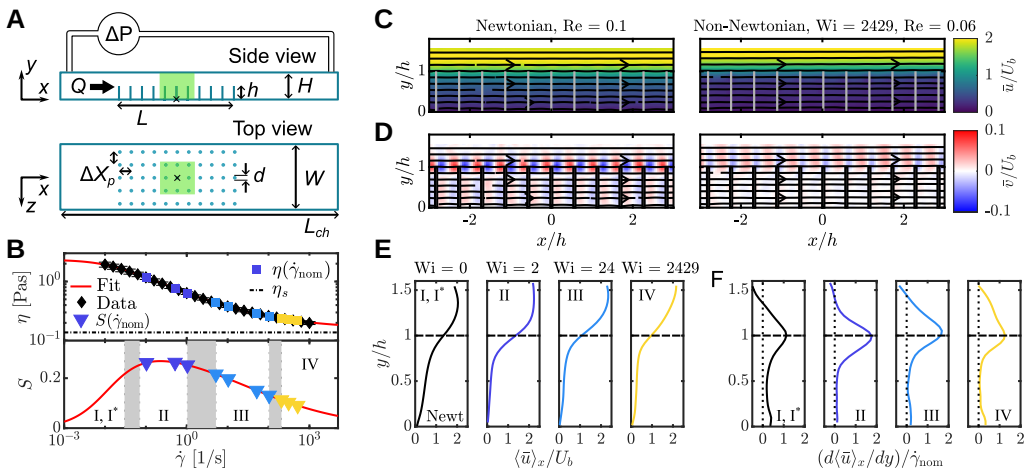

Fig. 1. Experimental setup, fluid properties, velocity field analysis, and flow regimes. A) Schematic representation of the experimental setup from both side and top views, highlighting key length scales. The setup features a rectangular microchannel made of fused silica with a regular array of pillars. The velocity field of a viscoelastic fluid was measured using micro-Particle Image Velocimetry (μ-PIV) with the green semitransparent rectangles depicting the field of view from both perspectives. The black crosses indicate the origin of the coordinate system. B) Rheological properties of the test fluid (partially hydrolyzed polyacrylamide dissolved in an 89.5:10.5 wt% glycerol/water solution). *Up*: Viscosity curve with the data in black diamonds, a Carreau–Yasuda fit with a red solid curve, the viscosity for the nominal shear rates ($\dot{\gamma}_{\mathrm{nom}}$) tested in squares, and the solvent viscosity with a dot-dashed black line. *Down*: Shear-thinning parameter, S, obtained from the fit to the viscosity curve. The triangles correspond to the shear thinning parameter at the nominal shear rate. Four flow regimes are marked, and the gray areas indicate the ranges within which the transitions between regimes could occur. The transitions between four distinct flow regimes are indicated, with regime I^* representing the expected low-Wi behavior observed only with the Newtonian fluid. C) Time-averaged streamwise velocity fields, $\bar{u}/U_b$, for both Newtonian and non-Newtonian fluids at the same flow rate (Q = 5 mL/min). D) Time-averaged wall-normal velocity fields, $\bar{v}/U_b$, for the same fluids and flow rate. E) Time and space-average velocity profiles for different Weissenberg numbers (Wi), with Wi = 0 the Newtonian case. F) Vertical derivatives of the velocity profiles shown in (E). The horizontal dashed lines mark the position of the canopy tips, while the vertical dotted lines serve as a reference for a vertical derivative equal to zero.

drawing analogies from classical turbulence, while acknowledging their fundamental differences (25). Despite the progress made, ET remains less understood than classical turbulence, particularly in complex configurations like canopy flows.

This study aims to bridge that gap by investigating the flow of a viscoelastic polymer solution within and above a microcanopy contained in a microfluidic channel, using insights from inertial canopy flows to inform our understanding of ET in these systems. We propose that similar to their inertial turbulent counterparts (6, 28), microscale canopy flows in the ET regime can be segmented spatially into distinct regions: a porous layer within the canopy, an effective mixing layer at the tips of the canopy, a transition layer above the canopy, and a layer of Poiseuille-like flow further up. This conceptual framework will help delineate the different flow regimes encountered as Wi increases, ultimately leading to instability and ET. By systematically varying Wi and examining the flow stability and structures, we aim to uncover deeper insights into ET's mechanisms and its potential applications in microfluidic design and real-world scenarios.

Results

We fabricated a transparent, straight microfluidic channel with a rectangular cross-section with height $H = 0.51$ mm and width $W = 3.7$ mm. The channel contained a rigid canopy consisting of square matrix of 23×123 pillars with height $h = 0.27$ mm, diameter $d = 0.015$ mm, and a spacing $\Delta X_p = 0.15$ mm as sketched in Fig. 1A. With those dimensions, the pillars do not bend under our flow conditions (Young's modulus $E = 73$ GPa (29), see Materials and methods) eliminating the need to consider the coupling between the flow and the movement of the pillars, which can make the analysis more complicated (30). Furthermore, we have a fully submerged and confined canopy, with a solidity factor $s_f = hd/(\Delta X_p)^2 = 0.17 \pm 0.005$. The latter is a parameter typically used in the inertial canopy community to differentiate between sparse ($s_f < 0.1$) and dense ($s_f > 0.1$) canopies.

The test fluid was a solution of partially hydrolyzed polyacrylamide (100 ppm, HPAA) in an 89.5 wt% glycerol/water solution, with a relaxation time of $\lambda = 4.7 \pm 0.4$ s measured by the capillary break-up method (31–33). The viscosity η, plotted in Fig. 1B, shows that the fluid was moderately shear-thinning and is well fitted with the Carreau–Yasuda model. The fit was used to calculate the shear thinning parameter S, which measures the importance of shear thinning and is shown at the bottom of Fig. 1B (the full definitions of the model and of S are in the Materials and methods). We used the glycerol/water solution without polymer as a reference Newtonian fluid with a viscosity $\eta_s = 0.14$ Pas. The small height of the channel was chosen to enable us to reach large $\mathrm{Wi} = \lambda\dot{\gamma}_{\mathrm{nom}}$, calculated using the nominal wall shear rate, $\dot{\gamma}_{\mathrm{nom}} = 6U_b/H$, with $U_b = Q/(HW)$ and Q the volumetric flow rate, considering an equivalent Poiseuille flow (33, 34) through a channel of height H. The Reynolds number was calculated as $\mathrm{Re} = \rho U_b H/\eta(\dot{\gamma}_{\mathrm{nom}})$, with $\rho = 1{,}230.7$ kg/m^3 the density of the solvent interpolated from literature values (35). $\mathrm{Re} \leq 0.1$ in all experiments and is therefore neglected throughout the remainder of the article.

In the following sections, we will consider a coordinate system as indicated in Fig. 1A. The instantaneous velocities (scalar) in the x, y, and z directions are denoted as u, v, and w, respectively. An overbar $\bar{\bullet}$ indicates a time average, brackets $\langle\bullet\rangle_\beta$ indicate an average in space along a given coordinate if $\beta =$ x, y, z, or an average over several instances of an event if $\beta = N$. The velocity fluctuations are defined as $u'(\mathbf{x}, t) = u(\mathbf{x}, t) - \bar{u}(\mathbf{x})$, and $u_{\mathrm{rms}}(\mathbf{x})$ is the corresponding root mean square value, similar for v and w. In the text, we will refer to the region around the upper part of the pillars ($y \sim h$) as the *canopy tips*, while the wall located at $y = H$ will be referred to as the *upper wall*.

Average velocity regimes with increasing Wi

We started by looking for the conditions at which the canopy flow becomes unstable. To achieve this, we measured the fluid velocity using micro-Particle Image Velocimetry (μ-PIV) at different flow rates with a Newtonian and a non-Newtonian fluid. The former served as a reference for laminar flows without elastic or shear-thinning effects. By measuring the flow at different downstream locations, we found that in general the flow is fully developed about 6 to 10 pillars downstream of the canopy, although at large Wi, the flow continues to evolve slowly further downstream (see Fig. S1 and the accompanying text in the Supplementary Information). The measurements presented here were done halfway downstream of the canopy inlet (the field of view was centered at pillar 67) to minimize possible end effects. When looking from the side view, the focal plane was parallel to the central row of pillars, i.e. at $z = 0$ (the field of view is sketched in the upper panel of Fig. 1A).

Two examples of the normalized time-averaged velocity fields in the horizontal, $\bar{u}/U_b$, and vertical direction, $\bar{v}/U_b$, are shown in Fig. 1C and D, respectively. The examples correspond to a Newtonian laminar flow and non-Newtonian unstable flow at the same flow rate. In both cases, the normalized streamwise velocity, $\bar{u}/U_b$, is approximately constant along x, with small periodic variations introduced by the presence of the pillars. These spatial variations are more evident for the vertical component, $\bar{v}/U_b$, (Fig. 1D) particularly for the Newtonian case. Nevertheless, the streamwise velocity is at least one order of magnitude larger than the vertical velocity. Therefore, we will focus on the time-space-average profiles of the horizontal component of the velocity.

We identified four distinct flow regimes with increasing Wi. The regimes are illustrated in Fig. 1E and F with four qualitatively different velocity profiles and are demarcated in the shear-thinning parameter plot in Fig. 1B. Regime I is the low-Wi steady laminar case, for which the flow outside the canopy has an approximately parabolic profile, i.e. a straight line in its derivative (in Fig. S2, we show a parabolic fit to the section of the profile outside the canopy). This regime is observed with the Newtonian fluid but not with the viscoelastic fluid due to limitations in the minimum attainable frame rate of our measurement system. However, we anticipate its appearance at sufficiently low Wi, so we have indicated it as I*. Regime II occurs at $\mathrm{Wi} \approx 1$, and corresponds to cases in which the velocity profile outside the canopy is flat. A flat profile is characteristic of shear-thinning fluids (36) so we call this regime the shear-thinning regime. Notice that the values of the shear thinning parameter S for these cases are the largest (purple triangles in Fig. 1B). Furthermore, we compared the velocity profile outside the canopy with that of an inelastic flow between parallel plates using the Carreau–Yasuda equation for the viscosity. In Fig. S2 of the Supplementary Material, we show that this model captures the measured behavior well. In Regime III (intermediate values of Wi), the velocity outside the canopy recovers a parabolic profile, indicating that shear-thinning effect has become less prominent (see Fig. S2). The cases in this regime correspond to the light blue triangles in Fig. 1B. Lastly, in regime IV, with $\mathrm{Wi} \approx 500$, the velocity profile outside the canopy deviates from the parabolic shape, with its derivative becoming convex and a slightly less pronounced peak at the canopy tips. As detailed in the next section, Regime IV is associated with ET, suggesting that the change in the profile results from the chaotic flow.

Despite their differences, all the profiles show a much faster velocity outside the canopy than inside it, resulting in a maximum velocity gradient at the tips of the canopy (see Fig. 1F), i.e. an inflection point. This observation is expected for $s_f > 0.1$ and will allow us to compare our results with inertial canopy flows that also have an inflection point at their tips.

Transition to ET

Having discussed the mean field characteristics of the flow we now turn to its velocity variations. Fig. 2A–C show the space-averaged Reynolds stresses normalized by the square of the bulk velocity. For the shear Reynolds stress, we took the absolute value before averaging in space, $\langle|\overline{u'v'}|\rangle_x/U_b^2$. The horizontal and shear Reynolds stresses increase significantly in regimes III and IV, while the vertical Reynolds stress barely changes with Wi, and it is homogeneous in space. This is in agreement with Ref. (25) where it was found that the most prominent velocity component in ET was the streamwise component. Additional support comes from top view measurements which show that the space average of the variations in the spanwise velocity, $\langle w_{\mathrm{rms}}\rangle_{x,z}$ are also small (see Fig. S3). The increase in $\langle\overline{u'u'}\rangle_x/U_b^2$ with Wi mainly occurs outside the canopy, but in regime IV, a slight increase is also observed within the canopy. The Reynolds stress follows a similar trend, but it is more sharply peaked. The increase in fluctuations in regimes III and IV indicates that the flow has become unstable.

To better illustrate the transition, Fig. 2D shows the plot of $\langle u^*_{\mathrm{rms}}\rangle_x/U_b = (\langle u_{\mathrm{rms}}\rangle_x - \langle u_{\mathrm{rms,Newt}}\rangle_x)/U_b$ vs. Wi. The fluctuations become larger than their Newtonian counterpart at large enough Wi, but depending on the vertical location, the deviation from the base noise happens at different Wi numbers. Outside and at the canopy tips, the fluctuations become large at $\mathrm{Wi}_{c,\mathrm{out}} \approx 24$, while inside the canopy, the increase is only noticeable for $\mathrm{Wi}_{c,\mathrm{in}} \approx 200$. This difference could be caused by the much smaller velocities and the shear rates within the canopy. By integrating the time-space averaged velocity profiles within the canopy ($0 < y < h$), we have calculated the local flux per unit length within the canopy, Q_{in}, and the local bulk velocity $U_{b,\mathrm{in}} = Q_{\mathrm{in}}/h \sim 0.3U_b$. Using this local bulk velocity, the critical Wi within the canopy decreases by approximately a half while the critical Wi outside the canopy becomes approximately 4 times larger, solving the discrepancy. Therefore, the Weissenberg number calculated using the local bulk velocity seems to be the control parameter determining the transition to unstable flow. However, since this value cannot be known a prior but must be measured experimentally, and given that the local bulk velocity outside the canopy is very close to the overall bulk velocity, $U_{b,\mathrm{out}} \sim 1.8U_b$, we will continue to use the Weissenberg number calculated using U_b in the reminder of this work.

The fluctuations at the canopy tips in Fig. 2D (squares) have a local maximum around $\mathrm{Wi} \sim 24$ before decaying slightly at $\mathrm{Wi} \sim 49$ and then increasing again (a similar trend is found for the fluctuations measured from the top view shown in Figs. S3 and S4). Such a local maximum in fluctuations has also been observed, for example, in porous media (37) and in experiments with single rows of pillars (38). Qin et al. (38) associated the first increase in fluctuations with the linear instability known to occur in viscoelastic flows with curved streamlines (39), which has also been observed in other works (24, 40, 41) with the critical Wi ranging from 1.6 to 3. On the other hand, the second increase in fluctuations was associated with a sub-critical transition at $\mathrm{Wi} \approx 9$. While the exact values are not the same, our data indicate that at the tips of the canopy, a first instability is caused by the curved streamlines (due to the circular cross-section of the pillars and their finite size), followed by a second instability of different nature and similar to that reported in Ref. (38). There are also curved streamlines

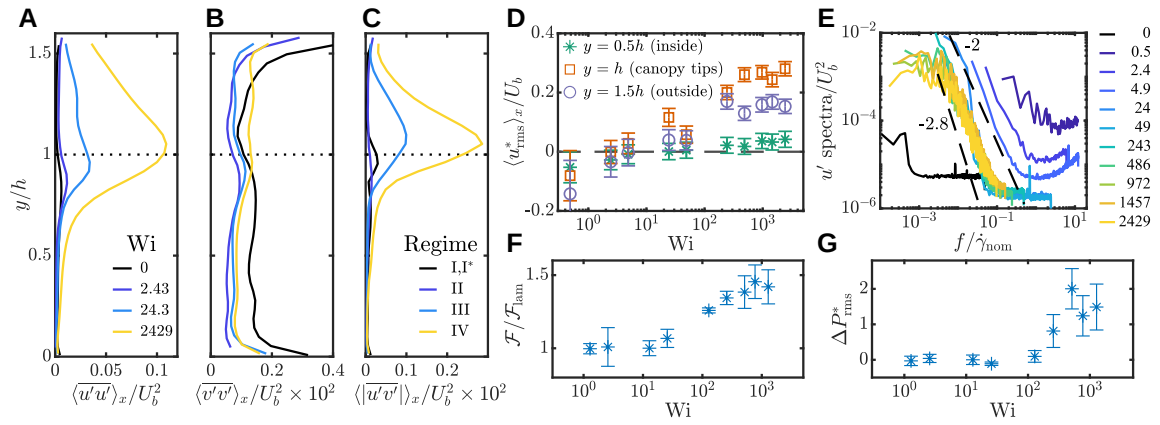

Fig. 2. Velocity fluctuations and pressure drop analysis. A–C) Space averaged profiles of the Reynolds stresses for the four cases presented in Fig. 1. In C), the space-averaged magnitude of the shear Reynolds stress is shown, because the sign alternates before and after each pillar, similar to the vertical velocity. D) Horizontal velocity fluctuations compensated by the Newtonian counterpart, $\langle u^*_{\rm rms} \rangle_x / U_b = (\langle u_{\rm rms} \rangle_x - \langle u_{\rm rms,Newt} \rangle_x)/U_b$, plotted against Wi. The different symbols indicate that fluctuations were measured inside, outside, and at the canopy tips. Error bars represent 1SD along the x direction. E) Temporal power spectra of the horizontal velocity fluctuations. The spectra were calculated at each position of the velocity field and then averaged along x. The spectra shown correspond to a location halfway outside the canopy ($y = 1.5h$). The legend indicates the Wi number. F) Friction factor normalized by its laminar counterpart $\mathcal{F}/\mathcal{F}_{\rm lam}$. The laminar regime was calculated as a linear fit to the first three data points. G) Fluctuations of the pressure drop normalized by the laminar regime, $\Delta P^*_{\rm rms} = \Delta P_{\rm rms}/\Delta P_{\rm rms,lam} - 1$. The laminar regime is calculated by a linear fit to the first five data points. The error bars in (F) and (G) correspond to 1SD over at least three repetitions.

inside the canopy, but as already mentioned, the much smaller flow speed within the canopy seems to mitigate the instability, at least at the same global Wi as at the canopy tips.

Shown in Fig. 2E are the temporal spectra of the streamwise velocity fluctuations at $y = 1.5h$ (approximately the middle point between the canopy tips and the upper wall of the channel). We also included the spectrum corresponding to the Newtonian case of Fig 1. The spectra are normalized by the bulk velocity and the frequency by the nominal shear rate, resulting in a collapse for the cases with Wi ≥ 24. These curves exhibit a region with an approximate power-law decay with the magnitude of their exponents between 2 and 2.8. Shnapp and Steinberg (21) found that in a straight channel with a smooth entrance, the magnitude of the exponent increases up to a value of 2 with Wi during what they called the transition regime. In the ET regime, the exponent continued to rise to around 2.8, and finally, in the drag reduction regime, it decreased to 2.2. A similar trend was observed in a straight channel with a nonsmooth inlet (16). In simulations of a straight channel flow with a fluid following the Phan-Thien–Tanner constitutive equation, the exponent was as low as 2 in what was considered the ET regime (25). Therefore, regime III can be considered transitional, while in regime IV the system has reached the ET state.

To further confirm the transition to ET, we measured the pressure drop, ΔP, along the whole channel (see Materials and methods for more details) from which we calculated the friction factor $\mathcal{F} = (2D_{\rm hyd}\Delta P)/(L\rho U_b^2)$, where $D_{\rm hyd} = 2HW/(H+W)$ is the hydraulic diameter of the channel without canopy. In Fig. 2F, we plotted the friction factor normalized by the laminar counterpart, $\mathcal{F}_{\rm lam} \propto Re^{-1}$, and in Fig. 2G, the pressure fluctuations $\Delta P_{\rm rms}/\Delta P_{\rm rms,lam} - 1$. Like in the case of a straight channel (16), both quantities increase above the laminar level at a large enough Wi number. The increase in the friction factor seems to start close to Wi ≈ 20, while in the pressure fluctuations, the increment is clear only above Wi ≈ 250, supporting the results of the power spectra.

Canopy flow in the ET regime

In this section, we focus on the case with Wi = 972 within the ET regime, referred to by De Blois et al. (27) as canopy ET. In Fig. 3A–C, we plotted three examples of coherent structures observed in the streamwise fluctuating velocity field. Specifically, we plot an average over several instances of the same event, $\langle u' \rangle_N$ normalized by U_b. In Fig. 3A, we show what we call a *stream*, in which all the fluctuating flow above the canopy moves in the same direction, either to the right or left. In Fig. 3B, we show elongated horizontal *stripes* within which u' has the same sign. In Fig. 3C, we show a *roller* that spans a few inter-pillar distances, ΔX_p. The rollers can have clockwise or counterclockwise rotation. The currents are the most common structure, while the rollers are the least. All the structures are advected downstream, with the rollers moving the slowest (see Movie 1 in the SI). It is tempting to associate the roller structures with a Kelvin–Helmholtz instability like in inertial canopy flows (2, 3). In the latter, the inflection point located at the canopy tips is the origin of the instability and of vortex shedding. While we also observe an inflection point, we do not have a prediction for the frequency of appearance of the rollers. Therefore, we cannot corroborate that the rollers are the result of a Kelvin–Helmholtz instability and their origin remains an open question. Concerning the stripes, they are reminiscent of those observed experimentally in straight channel flows (16, 42), and in simulations at the center of a straight channel (25) or around cylinders (40), suggesting that the flow above the canopy behaves similarly to a straight channel flow. It is not always clear how to differentiate between stripes and rollers; here, we define rollers as cases where the vertical velocity fluctuations are nonzero and change sign from the left half to the right half of the plot. In upcoming work, we plan to use Proper Orthogonal Decomposition and Spectral Proper Orthogonal Decomposition to better identify the structures and study how they get transported. Similar to how it was done recently for elastoinertial turbulence in channel flow (43).

We also performed several experiments by observing the flow in the microchannel from a top view. In Fig. 3E and F, we show two instantaneous snapshots of the streamwise velocity fluctuations, u'. These were obtained by positioning the focal plane outside the canopy, approximately midway between the upper wall of the channel and the canopy tips (refer to the sketch in Fig. 3D). We observed stripe-like structures accompanied by

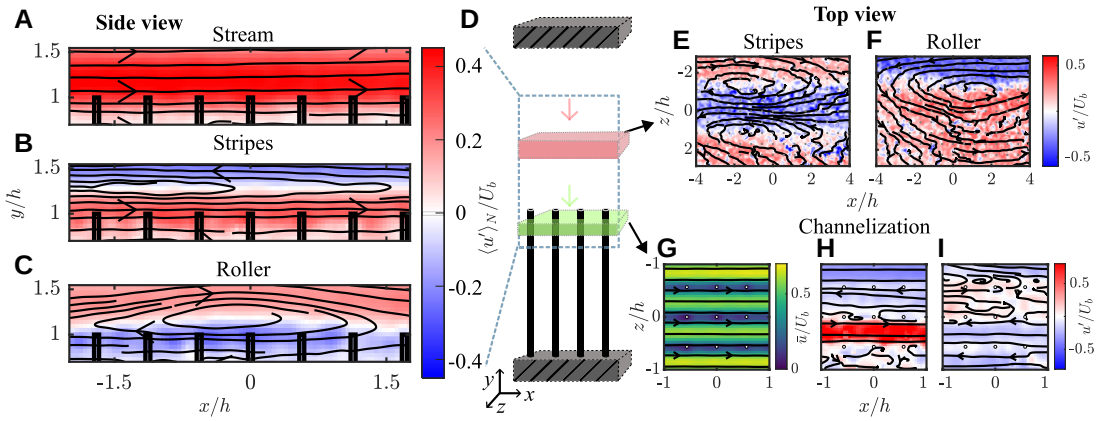

Fig. 3. Flow structures in the ET regime (Wi = 972). A–C) Examples of three coherent structures observed in the fluctuating velocity field obtained from the side view. A) What we call a *stream* in which the whole velocity field above the canopy has the same sign is shown. B) A pair of elongated *stripes*, and C) a *roller* are shown. For all three cases, we observed the equivalent structure with opposite signs (for the rollers, counterclockwise rotation). Each example represents an average over several instances of the same structure, indicated as $\langle u' \rangle_N$. Notice that the plots only show a reduced section of our field of view, indicated in the sketch in (D). The arrows in D) indicate the direction of observation for the top views. E and F) Examples of the instantaneous velocity fluctuation fields (u') showing large-scale stripe-like structures accompanied by a pair of rollers (E) and a larger roller (F). The gray dots indicate the location of the pillars. Notice that the pillars do not intersect with these fields of view. G–I) Streamwise velocity fields measured within the canopy and close to the tips. G) Time-averaged velocity field. H and I) Two instances of the instantaneous streamwise velocity fluctuations. The presence of the pillars causes the channelization of the flow and smaller structures in the fluctuation field (top of (I)). Notice the change in the zoom degree from (E and F) compared to (G–I). The circles indicate the location of the pillars.

rollers, as evidenced by the streamlines. In some cases, there were pairs of rollers, while in others, only single large rollers were visible within our field of view. Similar to the side view, these structures are significantly larger than ΔX_p. The channel dimensions seem to determine the size of these structures instead of the pillar diameter or spacing. Movie 2 in the SI shows the top-view velocity fluctuations and the advection of the structures. In some instances, the stripes form an angle with respect to the streamwise direction, x, resembling the waves observed in flexible canopies (27) or porous media (44, 45). However, the occurrence of the oblique stripes is not as common as the horizontal stripes shown in Fig. 3E. De Blois et al. (27) demonstrated that the appearance of the waves was independent of the flexibility of the pillars, and they occurred at Wi ~ 100, suggesting we should observe them in our system. Nonetheless, we rarely see waves with an oblique angle. A significant difference between De Blois' system and ours is the gap size between the canopy tips and the channel wall. In our setup, the gap is equal to the height of the canopy, while in (27), the gap was 24 times smaller than the canopy height. Given that waves have also been observed in porous media, where the pillars span the entire height of the channel (44, 45), we believe that having a small or no gap is crucial for eliciting waves or at least forming strong ones. With a larger gap, the flow has another dimension to deflect into (the observation of rollers from both side and top views indicates that the flow is 3D), whereas with a very small gap, the flow is virtually 2D. Therefore, the strong wave formation at an oblique angle might partly result from these dimensional constraints.

Figure 3G–I shows the flow within the canopy from the top view, very close to the canopy tips. The average flow in the streamwise direction is shown in Fig. 3G. It is evident that within the canopy, there are preferential flow paths in between each row of pillars, while there are stagnation zones downstream to each pillar. In Fig. 3H and I, we plotted two instantaneous fields of u', showing that the fluctuations mainly form coherent structures aligned with the preferential flow paths. The strong fluctuations can occur in single or multiple paths, with the rows of pillars creating sharp divisions in the flow. The pillars sometimes fragment the structures into smaller sizes, as observed in the uppermost row of pillars in the rightmost panel of Fig. 3I. Therefore, within the canopy, the inter-pillar distance and pillar diameter are the length scales determining the size of the flow structures, similar to what is observed in inertial canopies (28).

Coming back to the side view, while the focal plane is located at the central row of pillars, the depth of field (~ 70 μm) is thicker than the pillar's diameter, allowing us to observe focused particles in the same plane as the pillar's centers but also out of that plane. The particles out of the plane are more numerous and we corroborated that they are the ones that, after image processing, contribute more strongly to the velocity measurements. However, by a different image processing, we can extract the location of a few particles trapped in the slow wakes behind the pillars. Within those slow regions, the particles can move in any direction, even contrary to the direction of the main flow (see Movie 3 in the SI). The apparent random movement suggests that the flow behind pillars is shielded from the fast flow along the channels, similar to the flow between two obstacles in (22). In porous media, it has been shown that strands of highly stretched polymers form on the wake of the pillars (37, 44, 46, 47). These strands have been referred to as birefringent strands, and they can separate the flow into different sections of very different flow speeds, a phenomenon called channelization (46). While we do not have access to the stress field within the canopy, we can deduce that birefringent strands form around the pillars, promoting channelization and making the flow within the canopy very similar to that of porous media.

Canopy elastic vs. inertial turbulence

The flow structures discussed in the previous section showed that the velocity field within the canopy behaves differently from that outside it. Similar observations were reported for canopy inertial turbulence with high solidity factors, for which small vortices appeared within the canopy and large ones outside it (5, 6, 28). In this section, we compare our system with inertial canopy flows, using the latter as a reference to characterize the average velocity profiles we measured in the ET regime.

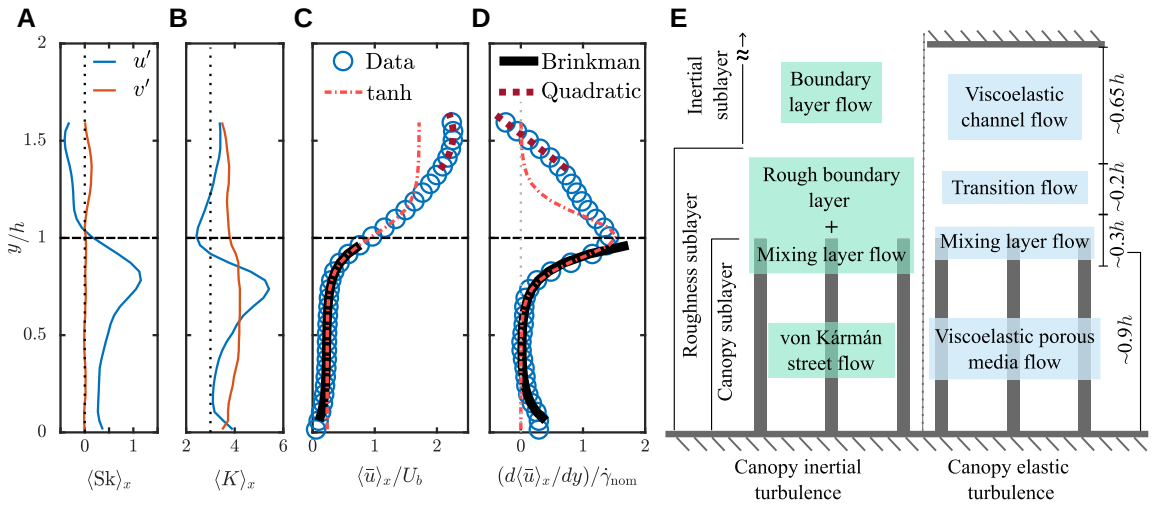

Fig. 4. Comparison of flow regions in ET (Wi = 972) and inertial canopy turbulence. A) Skewness and B) Kurtosis profiles of u' and v' averaged along x. The vertical dotted lines indicate a value of 0 or 3, respectively. C) Average velocity profile and D) its vertical derivative, with fits to different regions of the profiles. The dashed horizontal gray line marks the canopy tip location. E) Schematic comparison of flow regions in canopy inertial turbulence (left) and canopy ET (Wi = 972, right). The sketch illustrates different flow regions, with the leftmost labels applying only to the inertial canopy case. The roughness sublayer typically extends up to 2 or 3 times the canopy height, while the inertial sublayer continues indefinitely in terrestrial canopies or up to the water surface in aquatic canopies. The labels inside green boxes (left) indicate the different flow layers proposed by Poggi et al. (28), while the labels inside blue boxes (right) indicate the flow layers proposed in the present work for viscoelastic canopy flows in the ET state. The rightmost labels indicate the approximate sizes of each region in terms of h and specific for the experiment shown in (C and D).

As shown in Fig. 1D and E, all the velocity profiles exhibit an inflection point at the canopy tips ($y = h$) due to the drag caused by the canopy with a solidity factor $s_f > 0.1$. The inflection point originally motivated the analogy between the canopy inertial turbulent flows and the mixing layer flow (1, 2, 5, 6). Here, we test the same analogy for canopy ET. A useful quantity to support the analogy between mixing layers and inertial flows in dense canopies is the correlation coefficient, $r_{uv} = \overline{u'v'}/(u_{\mathrm{rms}} v_{\mathrm{rms}})$. This quantity typically reaches a maximum value of about 0.5 at the canopy tips, which is close to the 0.44 observed in mixing layers. However, this metric may not be the best to characterize ET. Foggi Rota et al. (48) calculated the joint probability functions of the fluctuating velocities in both Newtonian and viscoelastic channel flow simulations, revealing clear correlations between the velocity components in regular turbulence but not in ET. Therefore, we cannot expect r_{uv} to match the values in the inertial canopies. In fact, while our system's r_{uv} has a maximum at the canopy tips, its typical value is only about 0.34 (see Fig. S5), which is lower than that in a mixing layer. Therefore, we turn into other quantities like the space average skewness, $\langle Sk \rangle_x$, and kurtosis, $\langle K \rangle_x$, of u' and v', as plotted in Fig. 4A and B. The skewness and kurtosis of v' are almost constant along the vertical direction, supporting the idea that the streamwise velocity is the relevant component for ET. On the other hand, just below the canopy tips, $\langle \mathrm{Sk} \rangle_x$ of u' reaches a value close to 1 and changes its sign above the canopy, similar to a mixing layer. Additionally, the kurtosis exceeds 3 just below the canopy tips, reverting to 3 otherwise, mirroring measurements in inertial canopies by Poggi et al. (28).

Another test we conducted was to directly fit a mixing layer model to the average velocity profile, similar to the approach used by Zhang et al. (6) for urban canopies. Considering the region around the canopy tips and taking a few more data points within the canopy than above it, we fitted our data with a hyperbolic tangent function (49–51) given by

$$\langle \bar{u} \rangle_x(y) = 0.5 \Delta U \tanh[(y - y_{\mathrm{infl}})/l_{\mathrm{ML}}] + U_{\mathrm{infl}}, \quad (1)$$

where $\Delta U = 26.20$ mm/s, $U_{\mathrm{infl}} = 17.25$ mm/s, $y_{\mathrm{infl}} = 0.269$ mm, and $l_{\mathrm{ML}} = 0.041$ mm are fitting parameters and the numerical values correspond to those used in Fig. 4C and D. $\Delta U = U_f - U_{\mathrm{sl}}$ is the difference between the fast U_f and slow U_{sl} velocity streams in the mixing layer model. U_{infl} and y_{infl} are the speed and location of the inflection point, and l_{ML} is a characteristic length scale affecting the thickness of the mixing layer. This fitting worked well from about midway within the canopy up to $y = 1.15h$ (see the blue circles and the red dot-dashed line in Fig. 4D). We prioritized fitting the data within the canopy to ensure the fit's inflection point matched that of the data, consistent with Zhang et al. (6), who found that the mixing layer model works better within the canopy and in the vicinity of the canopy tips. Thus, for our viscoelastic canopy, the mixing layer model is also applicable within the region close to the canopy tips. Above $y \sim 1.15\,h$, the data deviates from the mixing layer model, while above $y \sim 1.35\,h$, it starts to follow a parabolic profile. The latter is corroborated by the quadratic fit (with coefficients $c_1 = -1.59 \times 10^3$ 1/mms, $c_2 = 1.30 \times 10^3$ 1/s, $c_3 = -0.23 \times 10^3$ mm/s) shown in Fig. 4C and D with a red dotted line. Despite being in the ET regime, the data away from the canopy remain parabolic, aligning with the results of Lellep et al. (25), where ET is achieved in a channel flow, and the mean profile is still parabolic except for a small deviation at the center of the channel. The presence of a transition zone between the mixing layer region and the parabolic region suggests that the instability originating from the canopy has a stronger effect on the mean flow than the instability from the center of a straight channel.

In the previous section, we showed evidence indicating that the flow within the canopy behaves like the flow in porous media. Therefore, inspired by works on hairy surfaces (9) and porous media (52), we have fitted the Brinkman equation to the velocity profile within the canopy,

$$\langle \bar{u} \rangle_x(y) = U_D(1 - e^{y/l_B}) + (U_s - U_D(1 - e^{h/l_B}))\frac{\sinh(y/l_B)}{\sinh(h/l_B)}, \quad (2)$$

where $U_D = 3.985$ mm/s, $U_s = 17.78$ mm/s, and $l_B = 0.026$ mm were used as fitting parameters while the height $h = 0.27$ mm of the canopy was imposed. The numerical values correspond to those used in Fig. 4C and D. U_D corresponds to Darcy's velocity, U_s to the slip velocity at the canopy tips, and l_B is a length scale affecting how flat the profile is within the canopy. The fit is fairly successful, almost up to the canopy tips, with a section overlapping with the mixing layer model. The fit captures the second inflection point within the canopy and accurately reflects the velocity approaching zero at the bottom wall, despite the Brinkman equation being suitable for Newtonian fluids. Consequently, we can conclude that within the canopy, the mean flow resembles that of a Newtonian fluid but with an effective viscosity greater than that of the solvent, given that the speed within the canopy is smaller than in the Newtonian case (see Fig. 1D).

In canopy inertial turbulence, it is well established that the flow can be divided into distinct regions or layers (1, 5, 6). In Fig. 4E, we have sketched a canopy and labeled the different layers conventionally used. The region going from the ground and up to the canopy tips is the canopy sublayer. The roughness sublayer extends to 2 or 3 times the height of the canopy and may include the canopy sublayer. This roughness sublayer is where the effects of the canopy significantly modify what would otherwise be a boundary layer flow over a smooth wall. Further up, there is the inertial sublayer, where the flow behaves as a classical boundary layer and can be divided into a logarithmic layer and a wake layer (6). Here, we consider it as the layer where the canopy effect is no longer felt.

Considering the coherent structures observed in dense canopies with inertial turbulence and different characteristic length scales, Poggi et al. (28) proposed a model to predict the vertical profile of the streamwise velocity. This model consists of three main components. First, deep inside the canopy sublayer, the flow is dominated by von Kármán street vortices. Second, around the canopy tips, the flow is characterized by a superposition of a rough-wall boundary layer and a mixing layer flow, which is susceptible to Kelvin–Helmholtz instabilities and the associated vortices. Third, above from the roughness sublayer, the flow transitions into a classical boundary layer flow. Keeping this model in mind and taking the results from this section and the previous one, we propose that our system can also be divided into different regions or layers as sketched on the right side of Fig. 4E. We have indicated the approximate sizes of each region in terms of h, specific to the experiment shown in Fig. 4C and D. Within the canopy, the pillar dimensions dictate the flow length scales. Instead of von Kármán vortices, we observe channelization and slow wakes behind the pillars, designating this region as the viscoelastic porous media flow. At the canopy tips, where fluctuations are the largest and the inflection point is located, there is an asymmetric mixing layer flow. Just above this, the flow profile deviates from the mixing layer model, which we term the transition region. Finally, away from the canopy, the flow resembles a channel flow with a parabolic profile. It is important to note that the boundary conditions away from the canopy differ in each case. In our system, there is a no-slip boundary condition. In inertial canopies, conditions vary: aquatic canopies have a stress-free condition, while terrestrial canopies have an unconstrained domain. Regardless, our point is that away from the canopy, the flow transitions into the conditions that would exist if the canopy were absent. In canopy inertial turbulence, this is a boundary layer; in canopy ET within a microfluidic device, it is a channel flow.

While we could have fitted the entire profile with the mixing layer model as done in Ref. (49), this approach would have displaced the model's inflection point upwards. By fitting the profile in sections, we suggest that the overall profile is a mixture of different models depending on the vertical direction. In future work, we plan to vary the canopy height to further corroborate this hypothesis.

Conclusion and outlook

We have studied the flow of a viscoelastic fluid within a microfluidic device containing a microcanopy. Our findings reveal that the mean flow undergoes four distinct regimes as the Wi number increases, with the fourth regime corresponding to ET.

We found evidence that the transition to canopy ET occurs in two steps: an initial increase in velocity fluctuations at intermediate Wi, followed by a decrease, and then a stronger increase at higher Wi, similar to some channel flows (38) and porous media flows (37). We confirm that in canopy flow, the streamwise velocity is the main unstable component, consistent with the channel flow simulations of Lellep et al. (25) and with the velocity decorrelation observed in ET by Foggi Rota et al. (48). Finally, in canopy ET, the velocity spectrum has an exponent closer to −3, similar to straight channel flows (16, 21) and viscoelastic jets (23), as opposed to the −4 exponent found in homogeneous isotropic ET (26), suggesting that the exponent could be sensitive to the isotropy of the flow.

In the ET regime, the flow behavior varies with the vertical location, displaying different coherent structures at each level. Consequently, we divided the canopy ET flow into distinct regions or layers, analogous to those used in inertial canopies (5, 6) and more specifically, those proposed by Poggi et al. (28). We identified a viscoelastic porous media flow within the canopy, a mixing layer flow at the canopy tips, a transition region just above the canopy, and a viscoelastic channel flow away from the canopy. In each region, except for the transition, we successfully fitted the average velocity profile using simple models: the Brinkman equation, a hyperbolic tangent, and a quadratic equation. Future work could explore more sophisticated models, such as the one developed by Ochoa-Tapia et al. (53), which considers spatial averages and could apply to the entire system.

In upcoming studies, we will vary the canopy height to observe how these regions are affected and if any of them disappear, especially in conditions where the gap above the canopy is much smaller than the heights of the canopy and the microchannel, aligning more closely with the work of De Blois et al. (27). In summary, canopy ET shares many features with inertial canopy flow despite the different underlying mechanisms.

We should stress that in the current work, the analogy to canopy inertial turbulence is serving as an inspiration on how to describe canopy ET. A proper connection between the two systems would require a more detailed investigation of the governing equations. The good description of the mean flow within the canopy and at its tips by the Brinkman equation and the mixing model for all Wi suggests the existence of some kind of self-similarity. Something that we are planning to pursue in the upcoming future.

It would also be interesting to test how mixing is affected by canopy ET. Recent studies have shown that elastic flow instabilities can enhance mixing and reaction kinetics in porous media (17) or heat transfer in microchannels (18, 19). We anticipate that similar effects could be achieved in the canopy, with the potential to adjust mixing by varying the canopy height, pillar spacing, or pillar diameter. Additionally, adjusting the channel-to-canopy height ratio could help mitigate the increased pressure drop caused by ET, thereby reducing the energy required to pump the liquid.

Materials and methods

Microfluidic channel and μ-PIV

A straight microfluidic channel was fabricated in fused silica using selective laser-induced etching (54). The channel had a length, width, and height of $L_{ch} = 48$ mm, $W = 3.65$ mm, and $H = 0.51$ mm, respectively. A microcanopy composed of a regular array of pillars spanned approximately two-fifths of the length of the channel starting about 1 cm downstream the inlet and extended over a length $L = 19.8$ cm. Figure 1A shows a sketch of the channel. The dimensions of the canopy result in a solidity factor of $s_f = hd/(\Delta X_p)^2 = 0.17 \pm 0.005$, where $d = 0.015$ mm and $h = 0.27$ mm are the diameter and height of the pillars, and $\Delta X_p = 0.15$ mm is the inter-pillar distance.

We consider the pillars to be rigid, given that fused silica has Young's modulus of $E = 73$ GPa (29), more than 10 times larger than the modulus of the flexible pillars used in (27). Moreover, if we use the Euler–Bernoulli beam theory like in Ref. (55), we can obtain an effective spring constant for each pillar according to $k = 8EI/h^3 = 77.1$ N/m, with $I = \pi d^4/4$ the second area moment for a circular cylinder. This spring constant is almost 10 times larger than for the pillars used in Ref. (55), indicating that in our case, the pillars are much more rigid. Within the resolution of our recordings (2 μm/pixel), we do not observe any movement of the tips of the pillars during our experiments.

We measured the velocity inside the channel using micro-Particle Image Velocimetry (μ-PIV) in straddle mode, seeding the flow with fluorescent particles (2 μm, R0200, Fluoromax, Fischer Scientific, aqueous solution). We measured velocity fields both from a side view (x – y plane) and a top view (x – z plane) of the channel. In the former case, the focal plane was located at the half-width of the channel (z = 0, depth of focus of 68 μ m, see Fig. 1A top). In the latter case, the focal plane was located at the canopy tips (depth of focus 12 μ m, see Fig. 3D) or halfway outside the canopy (depth of focus of 68 μ m, Fig. 3D). The flow was driven using a single syringe pump (Cetoni) from the inlet side. We did not use a second syringe pump at the outlet to avoid a contraction that resulted in recirculation and unstable flow (56) in initial designs. Therefore, the outlet was connected to a long, thick hose with a diameter larger than the channel's width and height, and with its end opened to the atmosphere.

Test fluid

We employed a viscoelastic solution of 89.5 wt% glycerol (e-Nacalai) and water (Milli-Q) with 100 ppm of partially hydrolyzed polyacrylamide (HPAA, 18 MDa, 70:30, Polyscience). We used the glycerol-water solvent as a Newtonian reference. The refractive index of the solution ($n_r = 1.4605$) was closely matched with that of the material of the channel. The solution was prepared by first making a buffer solution of HPAA in water and mixed it for at least 24 h. We then mixed part of the buffer with glycerol and the tracer particles. The solution was mixed using a roller mixer until the measured relaxation time was the same for samples taken from different locations within the mixture. The relaxation time of the fluid was measured to be $\lambda = 4.7 \pm 0.4$ s using the capillary break-up method (Haake CaBER). The CaBER device was fitted with plates of 6 mm in diameter, with an initial and final separation between the plates of 1 and 6 mm, respectively. The plates were separated at a constant speed of 25 mm/s.

The solution was stored in a cold room at 4 °C, and we measured its rheological properties before performing the experiments to corroborate that the solution had not deteriorated. The flow curve of the viscoelastic fluid was measured in a shear stress-controlled rheometer (MCR 502, Anton Paar) using a cone-plane geometry (1° angle at 25 °C). The top panel of Fig. 1B shows the plot of the viscosity vs. the shear rate. The solution has a moderate degree of shear thinning of about a 1-decade decrease in viscosity over 5 to 6 decades of shear rate. We fitted the data (black diamonds in Fig. 1B) with the Carreau–Yasuda model,

$$(\eta - \eta_\infty)/(\eta_0 - \eta_\infty) = [1 + (\dot{\gamma}/\dot{\gamma}^*)^a]^{((n-1)/a)},$$

where η, $\eta_0 = 2.33$ Pas, and $\eta_\infty = 0.16$ Pas are the viscosity, the zero shear viscosity, and the infinite-shear-rate viscosity, respectively. $\dot{\gamma}$ is the imposed shear rate, $\dot{\gamma}^* = 0.012$ 1/s is the characteristic shear rate for the onset of shear-thinning, $n = 0.66$ is the "power law exponent," and $a = 0.97$ is a nondimensional fitting parameter. The shear thinning parameter was calculated as $S = 1 - d\log\sigma/d\log\dot{\gamma}$, where $\sigma = \eta(\dot{\gamma})\dot{\gamma}$ is the shear stress (33, 57). The density of the liquid $\rho = 1{,}230.7$ kg/m^3 was interpolated from literature values (35).

Pressure drop measurements

To measure the pressure drop, we used a bidirectional pressure transducer (±15 psi, Omega) connected to the inlet and outlet of the channel via T-junctions. The total distance over which we measured the pressure drop was 15 cm, because of the T-junctions. However, our estimates indicate that the main pressure drop originates from the microfluidic channel, particularly under laminar flow conditions.

Acknowledgments

We gratefully acknowledge the support of the Okinawa Institute of Science and Technology Graduate University (OIST) and the Scientific Computing and Data Analysis (SCDA) section of the Research Support Division at OIST. R.A.L.C. thanks Cameron Hopkins for the initial designs of the microcanopy devices, Kazumi Toda Peters for helping with their fabrication, and Daniel W. Carlson, Giulio Foggi Rota, and Fabian Hillebrand for their valuable discussions.

Supplementary Material

Supplementary material is available at *PNAS Nexus* online.

Funding

This work is supported by funds from the Japan Society of the Promotion of Science (JSPS). R.A.L.C. under grant No. 23K19103. S.J.H. under grants No. 24K07332 and No. 24K00810. A.Q.S. under grant No. 24K00810.

Author Contributions

R.A.L.C.: Conceptualization, Methodology, Validation, Formal Analysis, Investigation, Data Curation, Writing—Original Draft Preparation, Writing—Review & Editing, Visualization, Project Administration, Funding Acquisition. S.J.H.: Conceptualization, Methodology, Resources, Writing—Review & Editing, Supervision, Funding Acquisition. A.Q.S.: Conceptualization, Methodology, Resources, Writing—Review & Editing, Supervision, Funding Acquisition.

Data Availability

All study data are included in the article and/or supporting information.

References

1 Finnigan J. 2000. Turbulence in plant canopies. *Annu Rev Fluid Mech*. 32(1):519–571.
2 Raupach MR, Finnigan JJ, Brunei Y. 1996. Coherent eddies and turbulence in vegetation canopies: the mixing-layer analogy. *Boundary Layer Meteorol*. 78(3-4):351–382.
3 Nepf HM. 2012. Flow and transport in regions with aquatic vegetation. *Annu Rev Fluid Mech*. 44(1):123–142.
4 Belcher SE, Harman IN, Finnigan JJ. 2012. The wind in the willows: flows in forest canopies in complex terrain. *Annu Rev Fluid Mech*. 44:479–504.
5 Brunet Y. 2020. Turbulent flow in plant canopies: historical perspective and overview. *Boundary Layer Meteorol*. 177(2-3):315–364.
6 Zhang W, Zhu X, Yang XIA, Wan M. 2022. Evidence for Raupach et al.'s mixing-layer analogy in deep homogeneous urban-canopy flows. *J Fluid Mech*. 944:A46.
7 Djenoune L, Berg K, Brueckner M, Yuan S. 2022. A change of heart: new roles for cilia in cardiac development and disease. *Nat Rev Cardiol*. 19(4):211–227.
8 Fliegauf M, Benzing T, Omran H. 2007. When cilia go bad: cilia defects and ciliopathies. *Nat Rev Mol Cell Biol*. 8:880–893.
9 Hosoi AE. 2019. Corrsin lecture on hairy hydrodynamics. *Phys Rev Fluids*. 4:110508.
10 Tamm SL. 1972. Ciliary motion in Paramecium. *J Cell Biol*. 55: 250–255.
11 Groisman A, Steinberg V. 2000. Elastic turbulence in a polymer solution flow. *Nature*. 405:53–55.
12 Groisman A, Steinberg V. 2001. Efficient mixing at low Reynolds numbers using polymer additives. *Nature*. 410:905–908.
13 Datta SS, *et al*. 2022. Perspectives on viscoelastic flow instabilities and elastic turbulence. *Phys Rev Fluids*. 7:080701.
14 Steinberg V. 2021. Elastic turbulence: an experimental view on inertialess random flow. *Annu Rev Fluid Mech*. 53:27–58.
15 Steinberg V. 2022. New direction and perspectives in elastic instability and turbulence in various viscoelastic flow geometries without inertia. *Low Temp Phys*. 48:492–507.
16 Li Y, Steinberg V. 2023. Universal properties of non-Hermitian viscoelastic channel flows. *Sci Rep*. 13(1):1064.
17 Browne CA, Datta SS. 2024. Harnessing elastic instabilities for enhanced mixing and reaction kinetics in porous media. *Proc Natl Acad Sci U S A*. 121:e2320962121.
18 Garg H, Wang L. 2024. Enhanced heat transfer in a two-dimensional serpentine micro-channel using elastic polymers. *Int J Thermofluids*. 23:100724.
19 Abed WM, Whalley RD, Dennis DJC, Poole RJ. 2016. Experimental investigation of the impact of elastic turbulence on heat transfer in a serpentine channel. *J Nonnewton Fluid Mech*. 231:68–78.
20 Fouxon A, Lebedev V. 2003. Spectra of turbulence in dilute polymer solutions. *Phys Fluids*. 15(7):2060–2072.
21 Shnapp R, Steinberg V. 2022. Nonmodal elastic instability and elastic waves in weakly perturbed channel flow. *Phys Rev Fluids*. 7(6):063901.
22 Varshney A, Steinberg V. 2019. Elastic Alfven waves in elastic turbulence. *Nat Commun*. 10:652.
23 Soligo G, Rosti ME. 2023. Non-Newtonian turbulent jets at low-Reynolds number. *Int J Multiph Flow*. 167:104546.
24 Qin B, Arratia PE. 2017. Characterizing elastic turbulence in channel flows at low Reynolds number. *Phys Rev Fluids*. 2(8): 083302.
25 Lellep M, Linkmann M, Morozov A. 2024. Purely elastic turbulence in pressure-driven channel flows. *Proc Natl Acad Sci U S A*. 121:e2318851121.
26 Singh RK, Perlekar P, Mitra D, Rosti ME. 2024. Intermittency in the not-so-smooth elastic turbulence. *Nat Commun*. 15(1):4070.
27 De Blois C, Haward SJ, Shen AQ. 2023. Canopy elastic turbulence: spontaneous formation of waves in beds of slender microposts. *Phys Rev Fluids*. 8:023301.
28 Poggi D, Porporato A, Ridolfi L, Albertson JD, Katul GG. 2004. The effect of vegetation density on canopy sub-layer turbulence. *Boundary Layer Meteorol*. 111:565–587.
29 McSkimin HJ. 1953. Measurement of elastic constants at low temperatures by means of ultrasonic waves-data for silicon and germanium single crystals, and for fused silica. *J Appl Phys*. 24:988–997.
30 Foggi Rota G, Monti A, Olivieri S, Rosti ME. 2024. Dynamics and fluid-structure interaction in turbulent flows within and above flexible canopies. *J Fluid Mech*. 989:A11.
31 Entov VM, Hinch EJ. 1997. Effect of a spectrum of relaxation times on the capillary thinning of a filament of elastic liquid. *J Nonnewton Fluid Mech*. 72:31–53.
32 Anna SL, McKinley GH. 2001. Elasto-capillary thinning and breakup of model elastic liquids. *J Rheol (N Y N Y)*. 45:115–138.
33 Haward SJ, Hopkins CC, Shen AQ. 2020. Asymmetric flow of polymer solutions around fluidic cylinders: interaction between shear-thinning and viscoelasticity. *J Nonnewton Fluid Mech*. 278: 104250.
34 Kundu PK, Cohen IM, Dowling DR, editors. Laminar flow. In: *Fluid Mechanics*. 5th ed. Academic Press, Boston, 2012. p. 309–359.
35 Volk A, Kähler CJ. 2018. Density model for aqueous glycerol solutions. *Exp Fluids*. 59(5):75.
36 Wang Y. 2022. Steady isothermal flow of a Carreau-Yasuda model fluid in a straight circular tube. *J Nonnewton Fluid Mech*. 310: 104937.
37 Haward SJ, Hopkins CC, Shen AQ. 2021. Stagnation points control chaotic fluctuations in viscoelastic porous media flow. *Proc Natl Acad Sci U S A*. 118:e2111651118.
38 Qin B, Salipante PF, Hudson SD, Arratia PE. 2019. Flow resistance and structures in viscoelastic channel flows at low Re. *Phys Rev Lett*. 123:194501.
39 Pakdel P, McKinley GH. 1996. Elastic instability and curved streamlines. *Phys Rev Lett*. 77:2459–2462.
40 Grilli M, Vázquez-Quesada A, Ellero M. 2013. Transition to turbulence and mixing in a viscoelastic fluid flowing inside a channel with a periodic array of cylindrical obstacles. *Phys Rev Lett*. 110: 174501.
41 Pan L, Morozov A, Wagner C, Arratia PE. 2013. Nonlinear elastic instability in channel flows at low Reynolds numbers. *Phys Rev Lett*. 110:174502.
42 Jha NK, Steinberg V. 2021. Elastically driven Kelvin-Helmholtz-like instability in straight channel flow. *Proc Natl Acad Sci U S A*. 118:e2105211118.
43 Kumar M, Graham MD. 2024. Nested travelling wave structures in elastoinertial turbulence. *J Fluid Mech*. 993:A8.
44 Ström OE, Beech JP, Tegenfeldt JO. 2023. Short and long-range cyclic patterns in flows of DNA solutions in microfluidic obstacle arrays. *Lab Chip*. 23:1779–1793.
45 Ström OE, Beech JP, Tegenfeldt JO. 2024. Geometry-dependent elastic flow dynamics in micropillar arrays. *Micromachines (Basel)*. 15:268.

46 Mokhtari O, Latché J-C, Quintard M, Davit Y. 2022. Birefringent strands drive the flow of viscoelastic fluids past obstacles. *J Fluid Mech*. 948:A2.
47 Mokhtari O, Quintard M, Davit Y. 2024. A web of sticky strands: how localized stress controls spatio-temporal fluctuations in viscoelastic flows through a lattice of obstacles. *J Fluid Mech*. 980:A7.
48 Foggi Rota G, Amor C, Le Clainche S, Rosti ME. 2024. Unified view of elastic and elasto-inertial turbulence in channel flows at low and moderate Reynolds numbers. *Phys Rev Fluids*. 9:L122602.
49 Marjoribanks TI, Hardy RJ, Lane SN, Parsons DR. 2017. Does the canopy mixing layer model apply to highly flexible aquatic vegetation? Insights from numerical modelling. *Environ Fluid Mech*. 17: 277–301.
50 Ghisalberti M, Nepf HM. 2002. Mixing layers and coherent structures in vegetated aquatic flows. *J Geophys Res Oceans*. 107(C2): 3-1.
51 Ghisalberti M, Nepf H. 2006. The structure of the shear layer in flows over rigid and flexible canopies. *Environ Fluid Mech*. 6: 277–301.
52 Chakrapani TH, Bazyar H, Lammertink RGH, Luding S, den Otter WK. 2022. The permeability of pillar arrays in microfluidic devices: an application of Brinkman's theory towards wall friction. *Soft Matter*. 19:436–450.
53 Ochoa-Tapia JA, Whitaker S. 1995. Momentum transfer at the boundary between a porous medium and a homogeneous fluid —I. Theoretical development. *Int J Heat Mass Transf*. 38: 2635–2646.
54 Burshtein N, Chan ST, Toda-Peters K, Shen AQ, Haward SJ. 2019. 3D-printed glass microfluidics for fluid dynamics and rheology. *Curr Opin Colloid Interface Sci*. 43:1–14.
55 Hopkins CC, Haward SJ, Shen AQ. 2020. Purely elastic fluid-structure interactions in microfluidics: implications for mucociliary flows. *Small*. 16(9):1903872.
56 Carlson DW, Shen AQ, Haward SJ. 2021. Microtomographic particle image velocimetry measurements of viscoelastic instabilities in a three-dimensional microcontraction. *J Fluid Mech*. 923:R6.
57 Haward SJ, McKinley GH. 2012. Stagnation point flow of wormlike micellar solutions in a microfluidic cross-slot device: effects of surfactant concentration and ionic environment. *Phys Rev E*. 85: 031502.